Japanese Journal of Applied Physics

The Japan Society of Applied Physics

RAPID COMMUNICATION

Influence of $BiFeO_3$ perovskite on the structure and magnetic properties of lead-free $Bi_{0.5}Na_{0.4}K_{0.1}TiO_3$ films

Japanese Journal of Applied Physics **60**, 010902 (2021) **RAPID COMMUNICATION**
https://doi.org/**10.35848/1347-4065/abcf0a**

Influence of $BiFeO_3$ perovskite on the structure and magnetic properties of lead-free $Bi_{0.5}Na_{0.4}K_{0.1}TiO_3$ films

Ngo Duc Quan[1,2*], Nguyen Duc Minh[2,3], and Guus Rijnders[3]

[1]*School of Engineering Physics, Hanoi University of Science and Technology, Hanoi 100000, Vietnam*
[2]*International Training Institute for Materials Science (ITIMS), Hanoi University of Science and Technology, No. 1 Dai Co Viet road, Hanoi 100000, Vietnam*
[3]*MESA + Institute for Nanotechnology, University of Twente, P. O. Box 217, 7500AE Enschede, The Netherlands*

[*]E-mail: quan.ngoduc@hust.edu.vn

Received September 10, 2020; revised November 26, 2020; accepted November 29, 2020; published online December 11, 2020

Lead-free (1-*x*)$Bi_{0.5}Na_{0.4}K_{0.2}TiO_3$-*x*$BiFeO_3$ (abbreviated as BNKT-*x*BFO) ferroelectric films with *x* in the range from 0.00 to 0.10, were synthesized by the chemical solution deposition technique on Pt/Ti/SiO_2/Si substrates. The microstructures and magnetic behaviors of BNKT-*x*BFO films were analyzed in detail as a function of BFO concentration. X-ray diffraction patterns indicated that BNKT-*x*BFO films were grown with a single-phase perovskite structure. The pure films showed an antiferromagnetic behavior. The magnetic properties of the films were gradually transferred from antiferromagnetic to ferromagnetic properties when BFO concentration was raised. The saturated magnetization (M_S) reached the highest value of 10.3 emu cm^{-3} at the BFO-doped concentration $x = 0.10$. Our work will contribute to illuminate the impact of BFO (ABO_3 perovskite structure) on the magnetic properties of BNKT materials at room temperature. © 2020 The Japan Society of Applied Physics

Multiferroic materials, that possess simultaneously magnetic and electronic behaviors have infiltrated everywhere in modern life and technology. The multifunctional, multiferroic materials are a key factor to miniaturizing electronic devices, an attractive trend of new generation technology. Based on the magnetoelectric property, a new type of device would be formed, such as an electric field-controlled magnetic memory system. Multiferroics are attractive because not only do they own both magnetic and ferroelectric properties but also these orders are coupled strongly with each other leads to additional functionality. However, it is difficult for the conditions obtaining both ferromagnetic and ferroelectric characteristics to occur at the atomic-level.[1,2)] Multiferroics seldom occur in nature. This is a large challenge in designing room-temperature multiferroic materials.

Recently, some ways were discovered to create multiferroic materials, for example, forming the composite and/or multilayer between lead-based $PbTiO_3$ ferroelectric materials with $CoFe_2O_4$ ferromagnetics.[3,4)] However, the large amount of lead in these materials not only causes many negative effects on the environment but also directly harms human health. Therefore, experts have dedicated considerable efforts to develop lead-free multiferroic materials.[5,6)] Lead-free Bi(Na,Ka)TiO_3 (BNKT) ferroelectric materials have increasingly attracted attention thanks to possessing Bi^{3+} with the polarizable ability similar to Pb^{2+} ion. Bi is an environmental-friendly metal and elicited almost safety to living organisms.[7)] Previous studies indicated that BNKT materials exhibit optimum properties at the morphotropic phase boundary (MPB), where it possesses simultaneous commixture of rhombohedral (R3c) and tetragonal (P4mm) symmetries.[8,9)] Its remnant polarization (P_r) and piezoelectric coefficient (d_{33}) reach relatively high values of 38 $\mu C\,cm^{-2}$ and 167 $pC\,N^{-1}$, respectively, while the electromechanical coupling coefficient (k_{33}) is 0.56.[10)] Especially, BNKT-based materials were found to possess ferromagnetic behavior at room temperature.[11,12)] However, magnetic and ferroelectric properties obtained in BNKT are quite poor and their mechanism has not been illuminated yet. Numerous studies have proven that doping other perovskites may enhance the electromechanical properties of BNKT.[9)] This improvement originated from the competition between different phases in the materials. Recently, $BiFeO_3$ bismuth ferrite (BFO), thanks to the rhombohedral symmetry with the high polarizable ability and special properties is one of the most potential candidates. Bismuth ferrite possesses two coupled orders at room temperature as the ferroelectric and ferromagnetic moments.[13,14)] Ramesh and his co-works successfully deposited epitaxial multiferroic thin films $BiFeO_3$ with the heterostructures that possess greatly enhanced multiferroic properties.[15)] These films exhibited a spontaneous polarization at room temperature and their magnetization surpassed that of the bulk. In this work, BFO is the selected perovskite for the following reasons: *i*/rhombohedral symmetry of BFO may cause competition and interaction with BNKT's one; *ii*/Ti^{4+} may be substituted by Fe^{3+} ion, causing distorted crystal structure due to difference of ionic radius; *iii*/Fe^{3+} is acceptor dopants at *B*-site, forming oxygen vacancies. We desire that these reasons will contribute to the enhancement of multiferroic behaviors of BNKT films.

(1-*x*)$Bi_{0.5}Na_{0.4}K_{0.1}TiO_3$-*x*$BiFeO_3$ (abbreviated as BNKT-*x*BFO) films were synthesized via chemical solution deposition on Pt/Ti/SiO_2/Si substrates. The impact of BFO on the microstructures and ferromagnetic properties of BNKT thin films was examined as a function of the BFO-doped concentration. Because pure BFO materials exist with major limitations, causing a decline of ferromagnetic and ferroelectric properties at room temperature. The first one is a large leakage current, contributed by Fe^{2+} and oxygen vacancies.[16)] Secondly, it is found to be difficult to synthesize single-phase BFO perovskite because impurity phases, such as $Bi_2Fe_4O_9$, Bi_2O_3, and $Bi_{25}FeO_{39}$, are likely to form in the treatment.[17)] Hence, BFO content was selected in the low range $x = 0$, 0.02, 0.04, 0.06, 0.08 and 0.10. We prepared the precursor solutions with a concentration of 0.4 $mol\,l^{-1}$ for BNKT-*x*BFO films from the initial materials, such as bismuth nitrate [$Bi(NO_3)_3.5H_2O$] (98%, Sigma-Aldrich), sodium nitrate $NaNO_3$ (99%, Sigma-Aldrich), potassium nitrate KNO_3 (99%, Sigma-Aldrich), titanium isopropoxide [$Ti(OC_4H_9)_4$] (99%, Sigma-Aldrich) and nine hydrated ferric nitrate [$Fe(NO_3)_3.9H_2O$] (99%, Sigma-Aldrich). The cosolvents

were used as acetic acid (CH_3COOH) and 2-methoxyethanol ($CH_3OCH_2CH_2OH$), while acetylacetone ($CH_3COCH_2COCH_3$) was chosen as the stabilizer and polymerizing agent. To compensate for the loss of metals during high-temperature calcining, it is added 10 mol% excess amount of KNO_3 and 20 mol% excess amount of $NaNO_3$. First, the starting materials were dissolved into acetic acid and 2-methoxyethanol. BNKT-*x*BFO films were synthesized via the following process: *i*/the 0.4 M precursor solution was coated onto Pt(111)/Ti/SiO_2/Si substrates by using spin coater at 4000 rpm for 30 s; *ii*/the film layer was dried at 150 °C for 5 min, then pyrolyzed at 400 °C for 10 min to remove the organic roots; *iii*/the steps (*i*/and *ii*/) were repeated until the films obtained the desired thickness of about 300 nm; *iv*/the calcination at 700 °C with a heating rate of 5 °C min^{-1} is occurred for 60 min to crystallize, in the air conditions. The crystal structures of the BNKT-*x*BFO films were determined by X-ray diffraction (XRD, Bruker D8 Advanced, Germany) with Cu-Kα cathode ($\lambda = 1.5406$ Å) radiation. The microstructures, such as surface morphology, surface roughness, and grain sizes of the films were observed with the atomic force microscope (AFM, Slover PRO, NT-MDT, Russia) or the field emission scanning electron microscope (FE-SEM, S-4800, HITACHI, Japan). The magnetic behaviors were characterized by using the vibrating sample magnetometer (VSM, 7404, Lake Shore, USA).

After calcination with a crystallization temperature of 700 °C during the incubation period of 60 min on Pt/Ti/SiO_2/Si substrates, BNKT-*x*BFO films were analyzed for XRD to decode the phase composition and crystal structure. Figure 1(a) illustrates the XRD patterns of BNKT-*x*BFO thin films in the 2θ ranges of 20–80°. All films belong to a single-phase perovskite, without strange peaks present. It is verified that the initial chemicals fully reacted, forming the desired compounds and fabricated films are not contaminated with other impurities. The peak 111 with the intensity is superior to all other peaks, characteristic for the Pt–coated substrate. Other peaks around diffraction angles 32.5°, 47.2°, 58.5°, and 71° are assigned to 110, 200, 211, and 220 orientations, respectively of the pseudo-cubic symmetry. Oddershede et al. observed that unpoled BNKT exhibits pseudo-cubic symmetry with a lattice parameter a = 3.905 Å.[18] Low diffraction lines of the films with $x = 0.10$ were identified as the contribution of impurity phases $Bi_2Fe_4O_9$ and Bi_2O_3.[17] The average crystalline sizes of BNKT-*x*BFO films calculated by using the Scherrer equation via the 200 preferred orientations of the XRD data.[19]

$$D = K\lambda/\beta\cos\theta \quad (1)$$

where constants such as D, K, λ, β, and θ are the grain size, Scherrer constant (theoretically, K is equal to 0.9), wavelength, FWHM, and Bragg angle, respectively. The D value, illustrated in Table I, increased moderately from 31.4 to 33.7 nm with an increase of BFO content. Figure 1(b) shows the enlarged XRD patterns in the 2θ ranges of 46.8°–47.9°, where the variation tendency of the 200 diffraction peak is clearly presented. It is clear that the 200 peak is transferred toward lower 2θ angles with the increase of BFO content. This shift may be derived from the following reasons. The first one is the extension of the crystal lattice, caused by the larger ionic radius at *B*-site when Ti^{4+} is substituted by Fe^{3+} ion ($R_{Fe}{}^{3+} = 0.645$ Å, $R_{Ti}{}^{4+} = 0.605$ Å).[20] The second cause is the extension stress resulting from the interaction between crystal structures with different lattice parameters of BNKT and BFO. Unpoled BNKT exhibits pseudo-cubic symmetry with a lattice parameter $a = 3.905$ Å.[18] While BFO crystals possess an *R*3*c* rhombohedral structure with lattice parameters of $a_r = 3.96$ Å, $\alpha_r = 89.4°$.[21]

2D-3D AFM images of BNKT-*x*BFO films are shown in Figs. 2(a)–2(f). AFM images with the scanning area 90 μm × 90 μm reveal the smooth surfaces without cracks being exposed. The AFM analysis also assists to determine the surface roughness of the films, a necessary parameter to evaluate the quality of the films. This parameter is considered through the root-mean-square (*RQ*) values, obtained by software in the AFM equipment. Table I shows the *RQ* values of the BNKT-*x*BFO films, which range from 16 nm to 9.2 nm. It can be found that the *RQ* value decreases as the BFO-doping concentration is raised. The smallest *RQ* value (9.2 nm) is obtained for the film with BFO concentration $x = 0.08$. Such small *RQ* values confirm that the BNKT-*x*BFO thin films exhibit good surface quality.

Figures 3(a)–3(f) show the FE-SEM images of BNKT-*x*BFO films with different BFO contents. The microstructure of all BNKT-*x*BFO thin films is relatively homogeneous with the crystalline particles being evenly distributed across the

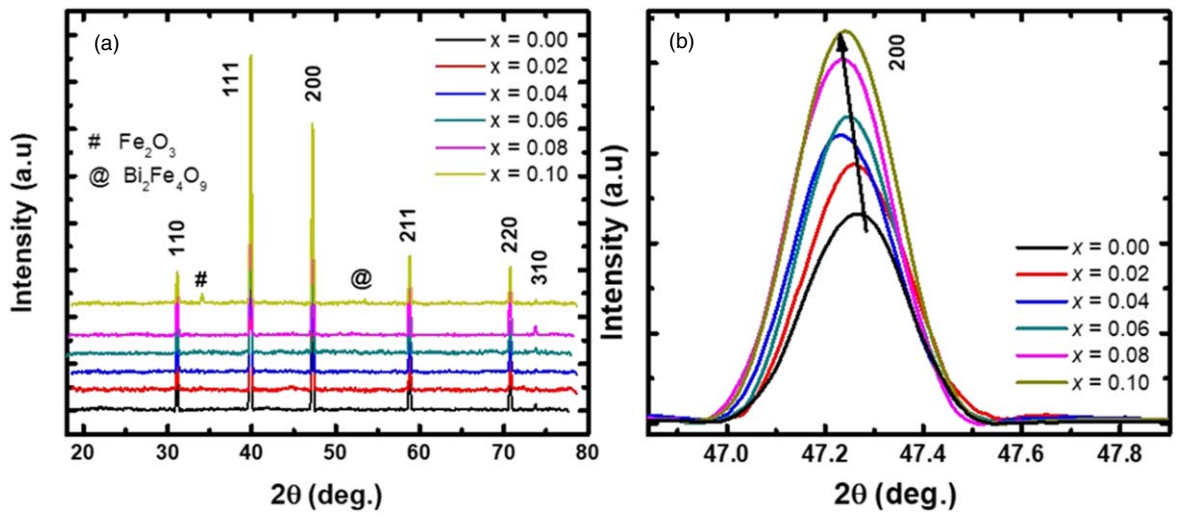

Fig. 1. (Color online) X-ray diffraction patterns of BNKT-*x*BFO thin films in the 2θ ranges of (a) 20°–80° and (b) 46.8°–47.9°.

Table I. Root-mean-square (*RQ*) and grain size (*D*) of the samples.

BNKT-*x*BFO	$x = 0.00$	$x = 0.02$	$x = 0.04$	$x = 0.06$	$x = 0.08$	$x = 0.10$
RQ (nm)	16.0	15.1	14.0	11.6	9.2	9.5
D (nm)	31.4	32.0	32.5	33.4	33.5	33.7

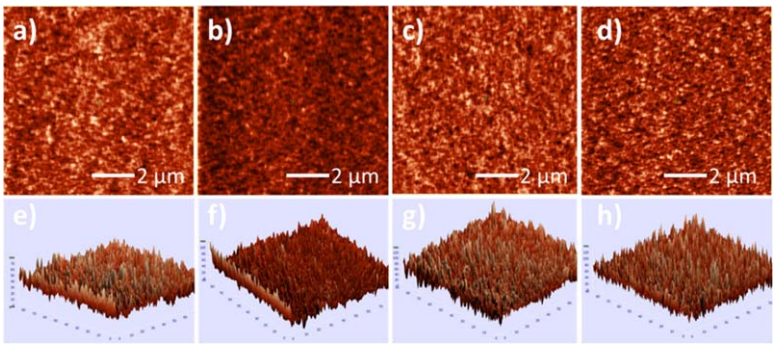

Fig. 2. (Color online) 2D–3D AFM images of BNKT-*x*BFO thin films (a) $x = 0.02$, (b) $x = 0.06$, (c) $x = 0.08$, and (d) $x = 0.10$.

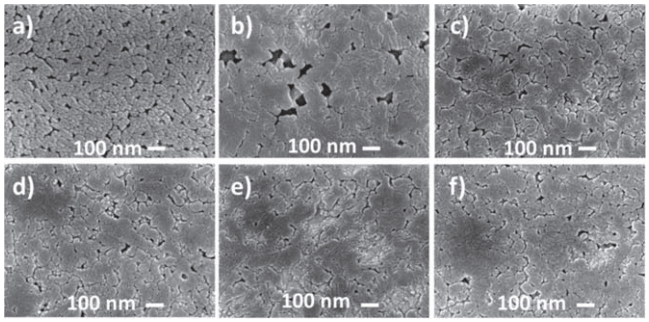

Fig. 3. FE-SEM images of BNKT-*x*BFO films: (a) $x = 0$, (b) $x = 0.02$, (c) $x = 0.04$, (d) $x = 0.06$, (e) $x = 0.08$, and (f) $x = 0.10$.

entire thin-film surface. On the thin-film surfaces appear some small holes, the cause is attributed to the rapid evaporation of organic roots. Another reason is that metals at the *A*-site (such as Bi^{3+}, Na^{+}, K^{+}) evaporate at high temperatures, forming oxygen vacancies.[22] It can be observed that when BFO-doped concentration increases, the average particle size is improved. This is explained as when doping BFO concentration increases, Fe^{3+} ions with a larger radius replace to Ti^{4+} position with a smaller radius at the *B*-site, causing a shift of the diffraction peaks and larger grain size. The microstructural analysis data in Figs. 2 and 3 show that the *RQ* value decreases as the BFO-doping concentration is raised, and the average particle size is improved. The improvement of microstructures is attributed to doping BFO that causes a decline of crystallization temperature. In previous work, we reported that the optimum crystallization temperature of BNKT films is 700 °C. While BFO is well crystallized with lower calcination temperatures from 400 °C to 600 °C.[23] This observation is consistent with the results being obtained from AFM images and XRD patterns above.

Figure 4 demonstrates the room-temperature magnetic hysteresis (*M–H*) loops of the BNKT-*x*BFO films with different BFO concentrations. The pure BNKT film exhibits the magnetic hysteresis (*M–H*) loops with the anti-*S*-shape and poor ferromagnetism at room temperature, contributed from the competition between antiferromagnetic and ferromagnetic orders. Hung et al. observed this behavior in BNT materials.[24] The $3d^{\circ}$ empty state of Ti^{4+} and/or the direct exchange coupling *B*-O-*B* (where *B* is Fe^{3+} and/or Ti^{4+}) are responsible for the antiferromagnetic properties in BNKT films.[20,25] BFO addition enhanced ferromagnetism of BNKT films at room temperature. When BFO is added into BNKT films, the antiferromagnetism is transferred to the ferromagnetism. The magnetic hysteresis (*M–H*) loops transform from the anti-*S*-shape to the *S*-shape. BNKT films with higher than 6 mol% BFO, the *M–H* loops reveal the *S*-shape of the ferromagnetic material. When the BFO concentration is increased, the magnetization of BNKT films is enhanced. For the films with a BFO-added concentration of 10 mol%, the saturation magnetization M_s reaches the highest value of around 10.3 emu cm^{-3} at 2 kOe. The remanent magnetization and coercive field possess values of around 1.9 emu cm^{-3} and 122 Oe, respectively. This provided the obvious evidence that BNKT-*x*BFO films possess ferromagnetic property at room temperature. We propose that this enhancement results from the super-exchange interaction of Fe^{3+} through oxygen vacancies ($V_{\ddot{O}}$). This interaction is formed from the random distribution of Fe^{3+} cations in the host lattice structure of BNKT. Hence, the magnetization may be derived from both surface effects and self-defect.[26] Coey et al. reported that the effective radius of hybrid orbital influences strongly the interaction of magnetic ions through oxygen vacancies.[24,27] Hence, the ferromagnetic interaction in the BNKT-*x*BFO films was improved due to Fe^{3+} cations controlling the interaction and distance of magnetic ions through oxygen vacancies. Figure 5 presents a schematic representation of the effects of the oxygen vacancy $V_{\ddot{O}}$ on the experimental magnetic ordering observed for BNKT films. The right part illustrates the electron interaction via oxygen atomic and vacancy states verifying the spin-orientation described in the left one. Weiss et al. reported that the mixing between transition metal 3*d* and oxygen 2*p* orbitals that enables virtual electron transfer between magnetic centers, causes the *B*-O-*B* (where *B* is Fe^{3+} and/or Ti^{4+}) antiferromagnetic exchange coupling.[28] This direct exchange coupling is responsible for the inverse spin arrangement neighboring the oxygen and causing antiferromagnetic behaviors. The substitution of Fe^{3+} ions at the Ti^{4+} sites will form oxygen vacancies, causing O(*p*)–Fe(*d*) hybridization as in dilute magnetic semiconducting

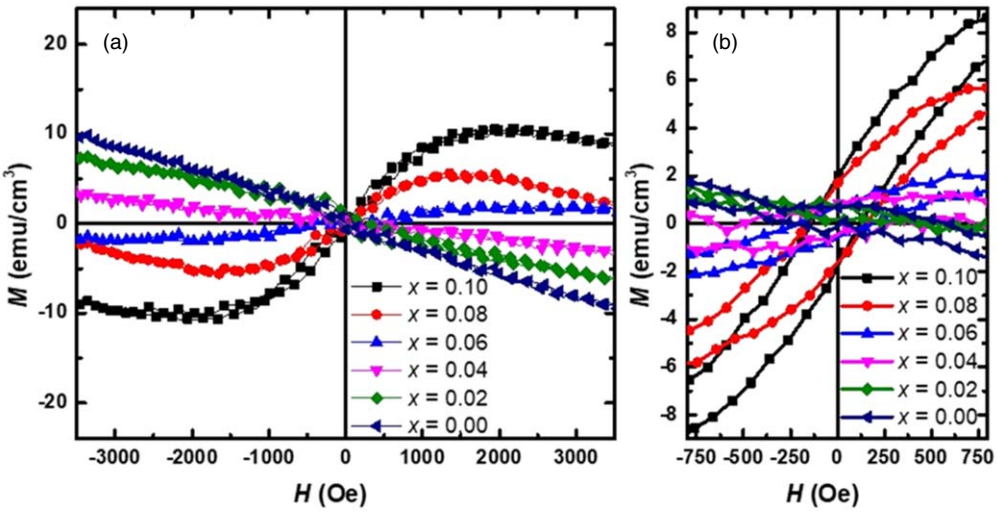

Fig. 4. (Color online) Magnetic hysteresis (M–H) curve of the BNKT-xBFO thin films with the applied magnetic field of 5 kOe at room temperature.

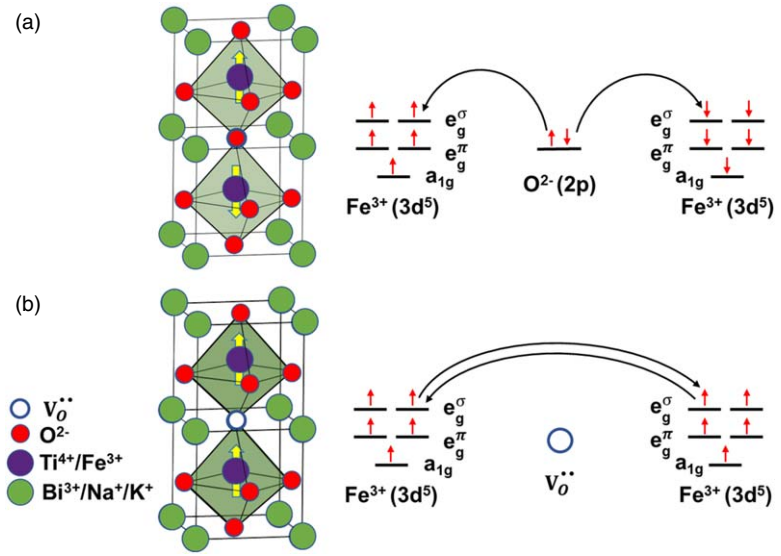

Fig. 5. (Color online) A schematic representation revealing the nature of antiferromagnetic and ferromagnetic orders in (a) original and (b) defective BNKT-BFO material. The right part illustrates the electron interaction mediated by oxygen atomic and vacancy states affirming the magnetic spin moment illustrated in the left one.

materials.[29] The charge carriers involved in bonding mediate the super-exchange interaction between the local spins via oxygen vacancies (Fe^{3+}–$V_{\ddot{O}}$–Fe^{3+}). The super-exchange interaction makes it possible for the magnetic moment neighboring oxygen vacancies to align in the same direction and forming ferromagnetic orders.

Sundaresan et al. believed that metal ions, such as Bi^{3+}, Na^{+}, K^{+} are likely evaporated during high-temperature treatment, forming the oxygen-deficient on the surfaces of the BNKT-xBFO films, and causing the magnetic moments.[22] Chemically, the Bi and Na/K loss can be described as follows:

$$\mathrm{Bi_{loss}} \rightarrow 2V_{Bi}''' + 3V_{\ddot{O}}, \tag{2}$$

$$(\mathrm{Na/K})_{\mathrm{loss}} \rightarrow 2V'_{N/K}V_{\ddot{O}}. \tag{3}$$

Where, V_{Bi}''' and $V'_{N/K}$ are point defects corresponding to Bi and Na/K loss; $V_{\ddot{O}}$ is oxygen vacancy. With Na/K deficiencies, defect combinations ($V_{N/K}'''$-$V_{\ddot{O}}$-$V'_{N/K}$) are formed.[30] The Bi loss can create the defect combinations $2(V_{Bi}'''$-$V_{\ddot{O}})'$-$V_{\ddot{O}}$, which is unlikely to occur because it needs a combination of five defects.[31] Based on theoretical studies, Stoneham and his co-workers have evidenced that point defects, as cation or anion vacancies contribute to magnetic moments.[32]

In conclusion, lead-free BNKT-xBFO films grown on Pt/Ti/SiO_2/Si substrates via a spin coating routine have been investigated for their microstructures and magnetic behaviors. All thin films show a single perovskite phase, without strange ones. When the BFO-added content is increased, the 200 peak is shifted toward lower angles because of the expansion of the perovskite lattice. This is contributed by the substitution of Fe^{3+} with the larger ionic radius for Ti^{4+} at the B-site. BFO addition enhanced ferromagnetism of BNKT films at room temperature. After BFO-doping, BNKT films converted from antiferromagnetism to ferromagnetism. With a BFO-added concentration of 0.10, the saturation magnetization M_s reaches the highest value of around 10.3 emu cm^{-3} at 2 kOe. The remanent magnetization and coercive field possess values of around

1.9 emu cm^{-3} and 122 Oe, respectively. This study provided an effective way to design multiferroic films from lead-free BNKT ferroelectric materials. Room-temperature ferromagnetism makes these BNKT-*x*BFO films possess more potential in multiferroic and spintronic applications.

Acknowledgments This research is funded by Nippon Sheet Glass Foundation and Vietnam National Foundation for Science and Technology Development (NAFOSTED) under Grant No. 103.02-2017.21.

ORCID iDs Ngo Duc Quan https://orcid.org/0000-0001-5654-7134

1) N. A. Spaldin and M. Fiebig, Science **309**, 391 (2005).
2) N. A. Hill, J. Phys. Chem. B **104**, 6694 (2000).
3) B. Y. Wang et al., RSC Adv. **3**, 7884 (2013).
4) M. Murakami, K. S. Chang, M. A. Aronova, C. L. Lin, M. H. Yu, J. H. Simpers, M. Wuttig, and I. Takeuchi, Appl. Phys. Lett. **87**, 112901 (2005).
5) W. Jo, R. Dittmer, M. Acosta, J. Zang, C. Groh, E. Sapper, K. Wang, and J. Rödel, J. Electroceramics. **29**, 71 (2012).
6) Y. Li, K. S. Moon, and C. O. Wong, Science **380**, 1419 (2005).
7) N. D. Quan, V. N. Hung, and D. D. Dung, J. Electron. Mater. **46**, 5814 (2017).
8) R. E. Eitel, A. R. Clive, R. S. Thomas, W. R. Paul, H. Wes, and P. Seung-Eek, Jpn. J. Appl. Phys. **40**, 5999 (2001).
9) N. D. Quan, L. Huu Bac, D. V. Thiet, V. N. Hung, and D. D. Dung, Adv. Mater. Sci. Eng. **2014**, 365391 (2014).
10) H. Yuji, W. Tomomi, N. Hajime, and T. Tadashi, Jpn. J. Appl. Phys. **47**, 7659 (2008).
11) Y. Wang, G. Xu, X. Ji, Z. Ren, W. Weng, P. Du, G. Shen, and G. Han, J. Alloys Compd. **475**, L25 (2009).
12) N. H. Tuan, D. V. Thiet, D. Odkhuu, L. H. Bac, P. V. Binh, and D. D. Dung, Physica B. Condens. Matter. **532**, 108 (2018).
13) J. R. Teague, R. Gerson, and W. J. James, Sol. Stat. Commun. **8**, 1073 (1970).
14) P. Fischer and M. Polomska, J. Phys. C. Sol. Stat. **13**, 1931 (1980).
15) J. Wang et al., Science **299**, 1719 (2003).
16) K. Y. Yun, M. Noda, M. Okuyama, H. Saeki, H. Tabata, and K. Saito, J. Appl. Phys. **96**, 3399 (2004).
17) J. Silva, A. Reyes, H. Esparza, H. Camacho, and L. Fuentes, Integr. Ferroelectr. **126**, 47 (2011).
18) J. Oddershede, M. Majkut, Q. Cao, S. Schmidt, J. P. Wright, P. Kenesei, and J. E. Daniels, J. Appl. Crystallogr. **48**, 882 (2015).
19) A. Monshi, M. R. Foroughi, and M. R. Monshi, World J. Nano Sci. Eng. **02**, 154 (2012).
20) L. T. H. Thanh, N. B. Doan, L. H. Bac, D. V. Thiet, S. Cho, P. Q. Bao, and D. D. Dung, Mater. Lett. **186**, 239 (2017).
21) L. Yan, H. Cao, J. Li, and D. Viehland, Appl. Phys. Lett. **94**, 132901 (2009).
22) A. Sundaresan, R. Bhargavi, N. Rangarajan, U. Siddesh, and C. N. R. Rao, Phys. Rev. B **74**, 161306 (2006).
23) D. Carranza-Celis, A. Cardona-Rodriguez, J. Narvaez, O. Moscoso-Londono, D. Muraca, M. Knobel, N. Ornelas-Soto, A. Reiber, and J. G. Ramirez, Sci. Rep. **9**, 3182 (2019).
24) N. T. Hung, L. H. Bac, N. N. Trung, N. T. Hoang, P. Van Vinh, and D. D. Dung, J. Magn. Magn. Mater. **451**, 183 (2018).
25) L. T. H. Thanh, N. B. Doan, N. Q. Dung, L. V. Cuong, L. H. Bac, N. A. Duc, P. Q. Bao, and D. D. Dung, J. Electron. Mater. **46**, 3367 (2017).
26) N. H. Tuan, L. H. Bac, L. V. Cuong, D. Van Thiet, T. Van Tam, and D. D. Dung, J. Electron. Mater. **46**, 3472 (2017).
27) J. M. D. Coey, M. Venkatesan, and C. B. Fitzgerals, Nat. Mater. **4**, 173 (2005).
28) A. Weiss and B. Bunsen, Phys. Chem. **68**, 996 (1964).
29) J. Chen, P. Rulis, L. Ouyang, S. Satpathy, and W. Y. Ching, Phys. Rev. B **74**, 235207 (2006).
30) Y. S. Sung, J. M. Kim, J. H. Cho, T. K. Song, M. H. Kim, H. H. Chong, T. G. Park, D. Do, and S. S. Kim, Appl. Phys. Lett. **96**, 022901 (2010).
31) Y. S. Sung, J. M. Kim, J. H. Cho, T. K. Song, M. H. Kim, and T. G. Park, Appl. Phys. Lett. **98**, 012902 (2011).
32) A. M. Stoneham, J. Gavartin, A. L. Shluger, A. V. Kimmel, D. M. Ramo, H. M. Rønnow, G. Aeppli, and C. Renner, J. Phys. Condens. Matter **19**, 255208 (2007).